

# Dynamics of Electron Injection in SnO<sub>2</sub>/TiO<sub>2</sub> Core/Shell Electrodes for Water-Splitting Dye-Sensitized Photoelectrochemical Cells

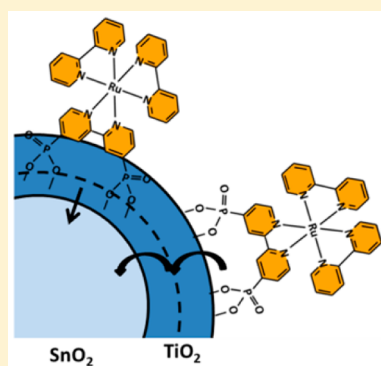
Nicholas S. McCool,<sup>†</sup> John R. Swierk,<sup>||</sup> Coleen T. Nemes,<sup>||</sup> Charles A. Schmuttenmaer,<sup>\*,||</sup> and Thomas E. Mallouk<sup>\*,†,‡,§</sup>

<sup>†</sup>Department of Chemistry, <sup>‡</sup>Department of Biochemistry and Molecular Biology, and <sup>§</sup>Department of Physics, The Pennsylvania State University, University Park, Pennsylvania 16802, United States

<sup>||</sup>Department of Chemistry and Energy Sciences Institute, Yale University, 225 Prospect Street, P.O. Box 208107, New Haven, Connecticut 06520-8107, United States

## S Supporting Information

**ABSTRACT:** Water-splitting dye-sensitized photoelectrochemical cells (WS-DSPECs) rely on photoinduced charge separation at a dye/semiconductor interface to supply electrons and holes for water splitting. To improve the efficiency of charge separation and reduce charge recombination in these devices, it is possible to use core/shell structures in which photoinduced electron transfer occurs stepwise through a series of progressively more positive acceptor states. Here, we use steady-state emission studies and time-resolved terahertz spectroscopy to follow the dynamics of electron injection from a photoexcited ruthenium polypyridyl dye as a function of the TiO<sub>2</sub> shell thickness on SnO<sub>2</sub> nanoparticles. Electron injection proceeds directly into the SnO<sub>2</sub> core when the thickness of the TiO<sub>2</sub> shell is less than 5 Å. For thicker shells, electrons are injected into the TiO<sub>2</sub> shell and trapped, and are then released into the SnO<sub>2</sub> core on a time scale of hundreds of picoseconds. As the TiO<sub>2</sub> shell increases in thickness, the probability of electron trapping in nonmobile states within the shell increases. Conduction band electrons in the TiO<sub>2</sub> shell and the SnO<sub>2</sub> core can be differentiated on the basis of their mobility. These observations help explain the observation of an optimum shell thickness for core/shell water-splitting electrodes.



Harnessing and converting solar energy into a useful form, for example, electricity or a chemical fuel, on a terawatt scale is among the most critical scientific challenges of the 21st century.<sup>1</sup> Natural photosynthesis does so, but with inherent efficiency limitations that can be surpassed in artificial systems.<sup>2</sup> In natural photosynthesis, a hierarchical assembly of light harvesting pigments funnel excitation energy into a reaction center, where a series of subnanosecond electron transfers occurs to yield a charge separated state with nearly 100% quantum efficiency.<sup>3–5</sup> Efficient charge transfer in natural photosynthesis relies on an optimized electron transfer cascade between the various donor and acceptor species. Achieving the same level of control over electron transfer events is a central goal of artificial photosynthesis, which seeks to develop artificial systems capable of using solar energy to photocatalytically drive water splitting and other fuel-forming endergonic reactions.<sup>6–8</sup>

Water-splitting dye-sensitized photoelectrochemical cells (WS-DSPECs) accomplish artificial photosynthesis by utilizing a semiconducting metal oxide film-sensitized with a molecular dye, which absorbs visible light and injects an electron into the oxide semiconductor. Holes diffuse across the surface via a series of lateral electron transfer events between dye molecules until they arrive at a catalytic site. This process repeats until the catalyst collects enough holes to oxidize water, generating molecular oxygen and four protons. The injected electrons diffuse through the electrode to a transparent conductive oxide

electrode and ultimately to a dark cathode where protons are reduced to hydrogen.<sup>9</sup>

Unfortunately, the quantum efficiencies of WS-DSPECs are only a few percent because hole transport and catalytic water oxidation are slow.<sup>10</sup> As a result, rapid recombination between the injected electron and the oxidized dye is the dominant mechanism for efficiency loss in these devices.<sup>11</sup> The use of visible light-absorbing dyes that are sufficiently oxidizing to drive water oxidation near neutral pH results in low injection yields into anatase TiO<sub>2</sub> ( $\eta_{inj} = 20\text{--}30\%$ ).<sup>11–13</sup> As an alternative, research on WS-DSPECs has focused on using SnO<sub>2</sub> as the electrode material.<sup>14,15</sup> SnO<sub>2</sub> has a conduction band minimum (CBM) several hundred millivolts below that of TiO<sub>2</sub>,<sup>13,16,17</sup> leading to improved injection yields.<sup>13</sup> The more positive CBM of SnO<sub>2</sub> also lowers the driving force for recombination. However, the rate of recombination has been found to be much faster for SnO<sub>2</sub> than for TiO<sub>2</sub> electrodes.<sup>17,18</sup>

One strategy for slowing down recombination while maintaining efficient injection is the use of a core/shell electrode architecture.<sup>19</sup> Recent work by Meyer and co-workers demonstrated a SnO<sub>2</sub>/TiO<sub>2</sub> core/shell structure prepared by atomic layer deposition (ALD) of TiO<sub>2</sub> on SnO<sub>2</sub> nanoparticles.

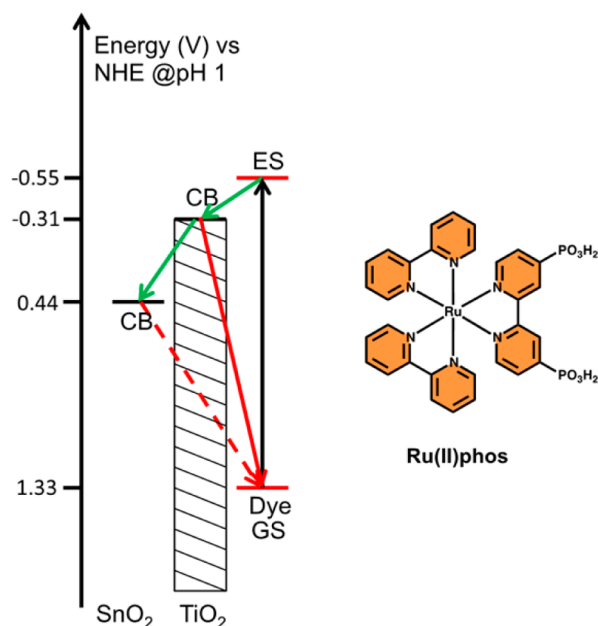
Received: July 13, 2016

Accepted: July 14, 2016

Published: July 14, 2016

This architecture results in an electron transfer cascade from the dye excited state into  $\text{TiO}_2$  and subsequently into the  $\text{SnO}_2$  CB, as shown in Scheme 1.<sup>14,15</sup> They observed efficient

**Scheme 1. Energy Diagram for the  $\text{SnO}_2/\text{TiO}_2$  Structure and Structure of  $\text{Ru(II)Phos}^a$**



<sup>a</sup>Potentials for ES and GS of  $\text{Ru(II)phos}$  taken from ref 21; for oxide, CBM taken from ref 16.

electron injection, slower recombination kinetics, and an overall enhancement in device performance. Knauf et al.<sup>20</sup> explored recombination with  $\text{TiO}_2$  shells of varying thickness on  $\text{SnO}_2$  and  $\text{ZrO}_2$ . Interestingly, they found that for shells thicker than 3.5 nm, electron recombination originated from localized electrons in the  $\text{TiO}_2$  shell, whereas for thinner shells recombination proceeded via a tunneling mechanism. Recently, we studied the ultrafast injection dynamics of sensitized bare- $\text{SnO}_2$  and  $\text{SnO}_2$  coated with 2.5 nm of  $\text{TiO}_2$  using time-resolved terahertz spectroscopy (TRTS).<sup>13</sup> In that study, we demonstrated that addition of the  $\text{TiO}_2$  markedly changed the injection kinetics. We suggested that an initial ultrafast injection component not apparent with bare  $\text{SnO}_2$  demonstrated injection into the  $\text{TiO}_2$  shell, followed by fast trapping and subsequent electron release into  $\text{SnO}_2$  on a much longer time scale. In this study, we revisit that system and use TRTS and steady state emission measurements to probe the electron injection process as a function of shell thickness.

Details of sample preparation are available in [Supporting Information](#). Briefly, we utilized atomic layer deposition (ALD) to prepare  $\text{TiO}_2$  shells of varying thickness on mesoporous  $\text{SnO}_2$ . ALD is a well-established technique for the deposition of conformal, atomically thin films of metal oxides on surfaces and has been used with great success in mesoporous structures.<sup>22,23</sup> Our previous work deposited 40 cycles of  $\text{TiO}_2$  on  $\text{SnO}_2$ , resulting in a film thickness of 2.5 nm as measured by deposition on a Si wafer.<sup>13</sup> This normalization infers a deposition of about 0.63 Å per cycle. In order to gain a better understanding of when shell material impacted charge injection, we varied the shell thickness from 1 to 40 pulse cycles, or a nominal thickness range of submonolayer coverage up to 2.5 nm. This deposition process was also carried out on porous

nanocrystalline  $\text{ZrO}_2$  films in order to probe how effectively the  $\text{TiO}_2$  shell alone with varying thicknesses could accept electrons from the dye.

Figure 1 shows the peak emission for both  $\text{SnO}_2/\text{TiO}_2$  and  $\text{ZrO}_2/\text{TiO}_2$  core/shell structures sensitized with bis(2,2-

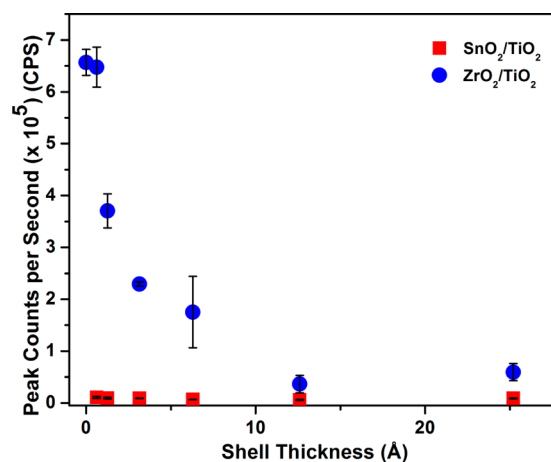


**Figure 1.** Peak emission intensity between 510 and 800 nm measured from  $\text{Ru(II)phos}$ -sensitized core/shell films with varying thicknesses of the  $\text{TiO}_2$  shell on a  $\text{SnO}_2$  core (red squares) and a  $\text{ZrO}_2$  core (blue circles). Emission was measured in  $\text{N}_2$ -purged, 0.1 M  $\text{HClO}_4$  (pH 1) aqueous solution.

bipyridine)(4,4-diphosphonato-2,2-bipyridine)ruthenium(II) bromide ( $\text{Ru(II)phos}$ ) at pH 1. Because both  $\text{SnO}_2$  and  $\text{TiO}_2$  accept electrons from the excited state of the dye, we anticipated significant emission quenching from injection into the  $\text{SnO}_2/\text{TiO}_2$  architecture at all thicknesses of  $\text{TiO}_2$ , as can be seen in Figure 1 (red squares). In the case of the  $\text{ZrO}_2/\text{TiO}_2$  samples, the  $\text{ZrO}_2$  core has a CBM well above the excited state potential of the dye and should not be able to quench the excited state of the dye. This can be seen in Figure 1 (blue circles) where there is significant emission intensity when the  $\text{TiO}_2$  shell is thin. With thicker  $\text{TiO}_2$  shells, the emission intensity decreases until  $\sim 13$  Å of  $\text{TiO}_2$ , after which it is similar to  $\text{SnO}_2/\text{TiO}_2$ . The complete quenching of the excited state demonstrates that at  $\geq 10$  Å of  $\text{TiO}_2$ , electron cascade through the shell completely controls the injection kinetics. Furthermore, the lack of emission quenching suggests that for shell thicknesses below  $\sim 2$  Å tunneling through the  $\text{TiO}_2$  dominates.<sup>24</sup> At intermediate thicknesses, a combination of tunneling and electron cascade may be occurring. In this size regime, quantum confinement effects can occur, resulting in an increase in the band gap and a shift of the CBM to more negative potentials.<sup>25</sup>

We can gain insight into the dynamics of injection by monitoring the ultrafast injection kinetics. Despite having a lower CBM energy (and as a result, a higher driving force for injection and lower driving force for recombination),  $\text{SnO}_2$  exhibits slow injection dynamics<sup>13,26,27</sup> when compared to  $\text{TiO}_2$ . The slow injection kinetics are a result of a low density of states (DOS) in the  $\text{SnO}_2$  CB,<sup>26</sup> which is comprised primarily of  $\text{Sn}^{4+}$  s and p orbitals,<sup>26</sup> whereas  $\text{TiO}_2$  has a high CB DOS made of  $\text{Ti}^{4+}$  d orbitals.<sup>28,29</sup> To understand the effect of  $\text{TiO}_2$  shell thickness on injection, we utilized TRTS, which is an ultrafast, far-infrared technique that is sensitive to changes in conductivity.<sup>13,30–33</sup> Electrons injected into mobile states (e.g., the conduction band) attenuate transmitted terahertz (THz)

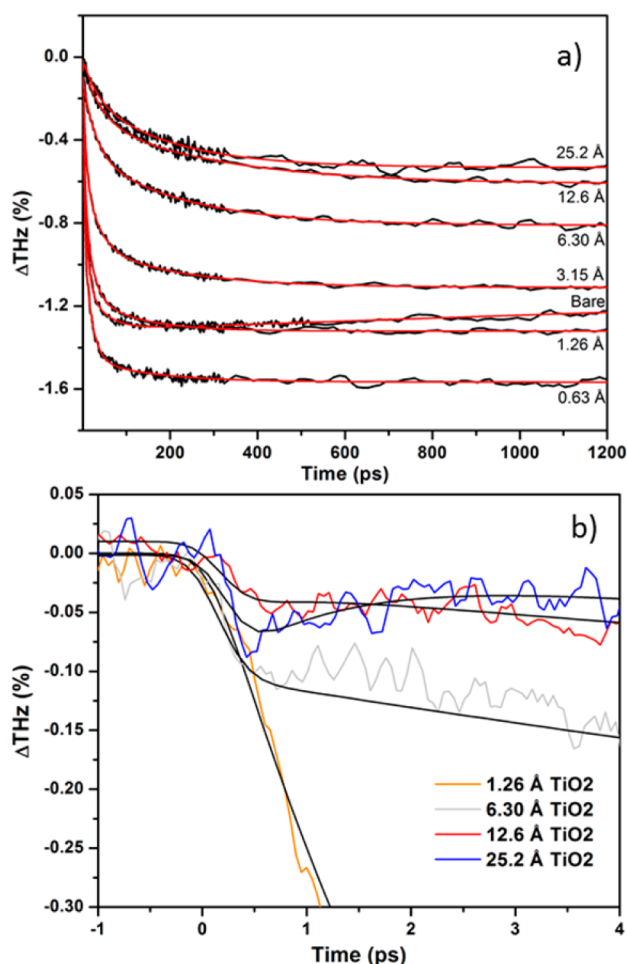


**Figure 2.** (a) Long time scale time-resolved THz spectroscopy (TRTS) traces for SnO<sub>2</sub>/TiO<sub>2</sub> electrodes with varying shell thicknesses. (b) Short time scale plot of the TRTS traces of a collection of samples from (a) in order to show the evolution of the initial injection into the TiO<sub>2</sub> shell with increasing thickness. TRTS scans were collected in a 0.1 M pH 1 HClO<sub>4</sub> aqueous solution.

radiation such that increases in conductivity following injection are observed as a decrease in the transmitted THz amplitude. Additionally, because the conductivity change depends in part on the electron mobility, TRTS is ideally suited for distinguishing whether the electron is located in the TiO<sub>2</sub>-shell or SnO<sub>2</sub>-core on the basis of the difference in electron mobility between the two materials.

Figure 2 shows the TRTS traces (black) and respective fits (red) using eq 1:

$$\Delta\text{THz} \left\{ \Delta\text{THz}_0 + \sum_{i=1}^n A_i \left[ \exp\left(-\frac{t-t_0}{\tau_i}\right) - 1 \right] \right\} \otimes G(\text{FWHM}) \quad (1)$$

where  $\Delta\text{THz}_0$  is the baseline before  $t = 0$ ,  $n$  is the number of exponentials included in the fit,  $t_0$  corresponds to the injection time (i.e.,  $t = 0$ ),  $A_i$  is the amplitude of a given component,  $\tau_i$  is the lifetime of a given component,  $G(\text{fwhm})$  is a Gaussian instrument response function (determined to be 0.5 ps) and  $\otimes$  represents a convolution. Full fitting parameters are summarized in Table S1. The injection component of all traces from bare SnO<sub>2</sub> to 6 Å of TiO<sub>2</sub> were successfully fit using a three exponential equation, though slow trapping dynamics observed

in the bare samples required a fourth exponential (with a negative amplitude to represent trapping) to be included in the fit. Films coated with 12.5 and 25 Å required a fourth exponential to accurately reproduce trapping which occurs in the initial (0–5 ps) dynamics.

Surprisingly, we observe a higher THz attenuation for samples coated with 0.63 and 1.26 Å of TiO<sub>2</sub> when compared to bare SnO<sub>2</sub>, corresponding to a higher density of mobile electrons in the SnO<sub>2</sub> film. In order to ensure that changes in THz attenuation with shell thickness are not a result of different dye loading (e.g., a lower dye loading due to blocked pores), UV/vis spectra were measured for all samples. A summary of dye loading is shown in Figure S1, which demonstrates that loading across all samples is nearly within experimental error of each other. In fact, thicker shells show slightly increased dye loading, and would therefore not be expected to show diminished injection amplitude based on dye loading alone. As the dye loading is nearly identical between these samples, we suggest that the increase in injection amplitude is related to passivation of nonmobile surface states. These nonmobile states are generally ascribed to uncoordinated metal centers and can act as acceptor states for charge injection and, as a result, will not be observed with TRTS. The process of injection into nonmobile surface states in aqueous electrolyte has been observed by others using sensitized ZnO<sub>2</sub><sup>34,35</sup> as well as in our previous work focused on proton-induced surface trap states, which also detailed the inability of TRTS to observe these electrons.<sup>36</sup> The passivation of these states is further supported by the lack of slow trapping in any of the ALD coated samples when compared to the bare SnO<sub>2</sub>. The slow decay in the TRTS trace for bare SnO<sub>2</sub> is suggestive of trapping into surface states, as none of the TiO<sub>2</sub>-coated samples exhibit any long time, slow loss of THz amplitude associated with trapping. Hupp and co-workers observed a similar passivation of surface states with ALD.<sup>24</sup>

The dynamics observed for the 25 Å sample agree very well with our previous report on this system.<sup>13</sup> In that report, we assigned the rapid (<0.5 ps) decrease and recovery of the THz amplitude from 0 to 5 ps as rapid injection into TiO<sub>2</sub> followed by trapping within the TiO<sub>2</sub> or at the TiO<sub>2</sub>/SnO<sub>2</sub> interface (Figure 2b), with release into the SnO<sub>2</sub> core at longer time scales. We can clearly distinguish an evolving ultrafast injection component for samples with a TiO<sub>2</sub> shell of 6 Å or more, which strongly suggests that electrons are injecting directly into the TiO<sub>2</sub> shell. By comparing the initial injection lifetime, injection shifts with increasing shell thickness from occurring with a lifetime of several picoseconds to being instrument limited at <0.5 ps, which is consistent with injection into TiO<sub>2</sub> being much faster than into SnO<sub>2</sub>. This is attributed to a higher DOS in the TiO<sub>2</sub> CB than in SnO<sub>2</sub> as described above.<sup>13</sup> A fast trapping component can be clearly distinguished with increasing shell thickness (Figure 2b), suggesting that the trapping sites are located in the TiO<sub>2</sub> shell and not at the SnO<sub>2</sub>/TiO<sub>2</sub> interface. This is also consistent with work by Knauf et al., who directly observed the recombination rate of electrons with oxidized Ru(II)phos in SnO<sub>2</sub>/TiO<sub>2</sub> structures and found that beyond a few nanometers, recombination occurs entirely from the TiO<sub>2</sub> shell.<sup>20</sup> As we noted in our previous work, after injection into the TiO<sub>2</sub> shell, the release kinetics from the shell into the core material are largely independent of shell thickness.<sup>13</sup>

Figure 3 shows the scaling factor and electron transfer rate,  $1/\langle\tau_w\rangle$ , where  $\tau_w$  is a weighted average of the injection lifetimes,

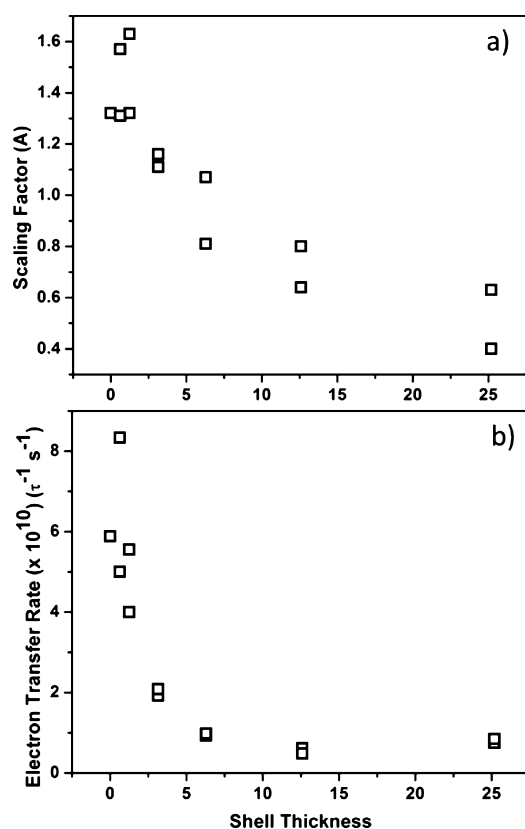


**Figure 3.** (a) Scaling factor and (b) weighted rate of electron transfer from fits to TRTS traces in Figure 2 for varying shell thicknesses.

as a function of shell thickness (Table S1). The scaling factor represents the overall injection yield of each trace and is a sum of the A components before normalization for each trace; the value is included in Table S1. This factor is directly proportional to the number of mobile electrons and thus by extension to the injection amplitude. Interestingly, we find that the rate of electron transfer becomes largely constant after approximately 5 Å of TiO<sub>2</sub>, which is consistent with steady state emission data for sensitized TiO<sub>2</sub>/ZrO<sub>2</sub>. This suggests that after 5 Å the excited state of the dye “senses” only the TiO<sub>2</sub> shell. It is surprising then that we do not also see a leveling of the scaling factor. One likely explanation is that as the TiO<sub>2</sub> shell increases in thickness more electrons are injected directly into nonmobile sites and therefore are invisible to TRTS. These electrons can directly recombine with oxidized dye molecules on the surface. The increase in trapping within the shell with increasing shell thickness observed in Figure 2b supports that hypothesis.

Though TRTS has been used to probe core/shell nanostructures,<sup>37,38</sup> this and our previous study<sup>13</sup> are the first to explicitly follow the movement of an electron through the shell and into the core, demonstrating the power of TRTS for these types of architectures. By varying the thickness of the TiO<sub>2</sub> shell, we were able to demonstrate that electron injection proceeds directly into the SnO<sub>2</sub> core when the TiO<sub>2</sub> shell is less than 5 Å, but when the thickness is greater than 5 Å, it is injected first into the TiO<sub>2</sub> shell and then moves to the SnO<sub>2</sub> core. Furthermore, we were able to demonstrate that trapping of carriers into nonmobile sites occurs specifically within the TiO<sub>2</sub> shell. The degree of trapping in the shell increases with increasing shell thickness, further demonstrating the need to

balance injection and recombination dynamics through an optimal shell thickness.

## ■ ASSOCIATED CONTENT

### Supporting Information

The Supporting Information is available free of charge on the ACS Publications website at DOI: 10.1021/acs.jpcllett.6b01528.

Experimental details, fitting parameters for TRTS traces, and UV/vis data for dye surface coverage. (PDF)

## ■ AUTHOR INFORMATION

### Corresponding Authors

\*E-mail: charles.schmittenmaer@yale.edu. Phone: (203) 432-3915.

\*E-mail: tem5@psu.edu. Phone: (814) 863-9637.

### Notes

The authors declare no competing financial interest.

## ■ ACKNOWLEDGMENTS

We thank Svante Hedström for his suggestions during the preparation of the manuscript. This work was supported by the Office of Basic Energy Sciences, Division of Chemical Sciences, Geosciences, and Energy Biosciences, Department of Energy, under contracts DE-FG02-07ER15911 and DE-FG02-07ER15909 as well as by a generous donation from the TomKat Charitable Trust. N.S.M. thanks the National Science Foundation for support as a graduate fellow under Grant DGE1255832. Instrumentation and facilities used in this project were supported by the Pennsylvania State University Materials Research Institute Nanofabrication Laboratory under National Science Foundation Cooperative Agreement ECS-0335765.

## ■ REFERENCES

- (1) Lewis, N. S.; Nocera, D. G. Powering the Planet: Chemical Challenges in Solar Energy Utilization. *Proc. Natl. Acad. Sci. U. S. A.* **2006**, *103* (43), 15729–15735.
- (2) Neelson, K. H.; Conrad, P. G. Life: Past, Present and Future. *Philos. Trans. R. Soc., B* **1999**, *354* (1392), 1923–1939.
- (3) Moore, G. F.; Brudvig, G. W. Energy Conversion in Photosynthesis: A Paradigm for Solar Fuel Production. *Annu. Rev. Condens. Matter Phys.* **2011**, *2* (1), 303–327.
- (4) Blankenship, R. E.; Tiede, D. M.; Barber, J.; Brudvig, G. W.; Fleming, G.; Ghirardi, M.; Gunner, M. R.; Junge, W.; Kramer, D. M.; Melis, A.; et al. Comparing Photosynthetic and Photovoltaic Efficiencies and Recognizing the Potential for Improvement. *Science* **2011**, *332* (6031), 805–809.
- (5) Grabolle, M.; Dau, H. Energetics of Primary and Secondary Electron Transfer in Photosystem II Membrane Particles of Spinach Revisited on Basis of Recombination-Fluorescence Measurements. *Biochim. Biophys. Acta, Bioenerg.* **2005**, *1708* (2), 209–218.
- (6) Gust, D.; Moore, T. A.; Moore, A. L. Solar Fuels via Artificial Photosynthesis. *Acc. Chem. Res.* **2009**, *42* (12), 1890–1898.
- (7) Wasielewski, M. R. Self-Assembly Strategies for Integrating Light Harvesting and Charge Separation in Artificial Photosynthetic Systems. *Acc. Chem. Res.* **2009**, *42* (12), 1910–1921.
- (8) Kärkäs, M. D.; Johnston, E. V.; Verho, O.; Åkermark, B. Artificial Photosynthesis: From Nanosecond Electron Transfer to Catalytic Water Oxidation. *Acc. Chem. Res.* **2014**, *47* (1), 100–111.
- (9) Swierk, J. R.; Mallouk, T. E. Design and Development of Photoanodes for Water-Splitting Dye-Sensitized Photoelectrochemical Cells. *Chem. Soc. Rev.* **2013**, *42* (6), 2357–2387.
- (10) Zhao, Y.; Swierk, J. R.; Megiatto, J. D.; Sherman, B.; Youngblood, W. J.; Qin, D.; Lentz, D. M.; Moore, A. L.; Moore, T.

- A.; Gust, D.; et al. Improving the Efficiency of Water Splitting in Dye-Sensitized Solar Cells by Using a Biomimetic Electron Transfer Mediator. *Proc. Natl. Acad. Sci. U. S. A.* **2012**, *109* (39), 15612–15616.
- (11) Swierk, J. R.; McCool, N. S.; Mallouk, T. E. Dynamics of Electron Recombination and Transport in Water-Splitting Dye-Sensitized Photoanodes. *J. Phys. Chem. C* **2015**, *119* (24), 13858–13867.
- (12) Swierk, J. R.; Méndez-Hernández, D. D.; McCool, N. S.; Liddell, P.; Terazono, Y.; Pahk, I.; Tomlin, J. J.; Oster, N. V.; Moore, T. A.; Moore, A. L.; et al. Metal-Free Organic Sensitizers for Use in Water-Splitting Dye-Sensitized Photoelectrochemical Cells. *Proc. Natl. Acad. Sci. U. S. A.* **2015**, *112* (6), 1681–1686.
- (13) Swierk, J. R.; McCool, N. S.; Nemes, C. T.; Mallouk, T. E.; Schmittenmaer, C. A. Ultrafast Electron Injection Dynamics of Photoanodes for Water-Splitting Dye-Sensitized Photoelectrochemical Cells. *J. Phys. Chem. C* **2016**, *120* (11), 5940–5948.
- (14) Wee, K.-R.; Sherman, B. D.; Brennaman, M. K.; Sheridan, M. V.; Nayak, A.; Alibabaei, L.; Meyer, T. J. An Aqueous, Organic Dye Derivatized SnO<sub>2</sub>/TiO<sub>2</sub> Core/shell Photoanode. *J. Mater. Chem. A* **2016**, *4* (8), 2969–2975.
- (15) Sherman, B. D.; Ashford, D. L.; Lapidés, A. M.; Sheridan, M. V.; Wee, K. R.; Meyer, T. J. Light-Driven Water Splitting with a Molecular Electroassembly-Based Core/Shell Photoanode. *J. Phys. Chem. Lett.* **2015**, *6* (16), 3213–3217.
- (16) Grätzel, M. Photoelectrochemical Cells. *Nature* **2001**, *414* (6861), 338–344.
- (17) Green, A. N. M.; Palomares, E.; Haque, S. A.; Kroon, J. M.; Durrant, J. R. Charge Transport versus Recombination in Dye-Sensitized Solar Cells Employing Nanocrystalline TiO<sub>2</sub> and SnO<sub>2</sub> Films. *J. Phys. Chem. B* **2005**, *109* (25), 12525–12533.
- (18) Kamat, P. V.; Bedja, I.; Hotchandani, S.; Patterson, L. K. Photosensitization of Nanocrystalline Semiconductor Films. Modulation of Electron Transfer between Excited Ruthenium Complex and SnO<sub>2</sub> Nanocrystallites with an Externally Applied Bias. *J. Phys. Chem.* **1996**, *100* (12), 4900–4908.
- (19) Lee, S. A.; Zhao, Y.; Hernandez-Pagan, E. A.; Blasdel, L.; Youngblood, W. J.; Mallouk, T. E. Electron Transfer Kinetics in Water Splitting Dye-Sensitized Solar Cells Based on Core-shell Oxide Electrodes. *Faraday Discuss.* **2012**, *155*, 165–179.
- (20) Knauf, R. R.; Kalanyan, B.; Parsons, G. N.; Dempsey, J. L. Charge Recombination Dynamics in Sensitized SnO<sub>2</sub>/TiO<sub>2</sub> Core/Shell Photoanodes. *J. Phys. Chem. C* **2015**, *119* (51), 28353–28360.
- (21) Hanson, K.; Brennaman, M. K.; Ito, A.; Luo, H.; Song, W.; Parker, K. A.; Ghosh, R.; Norris, M. R.; Glasson, C. R. K.; Concepcion, J. J.; et al. Structure–Property Relationships in Phosphonate-Derivatized, Ru II Polypyridyl Dyes on Metal Oxide Surfaces in an Aqueous Environment. *J. Phys. Chem. C* **2012**, *116* (28), 14837–14847.
- (22) Dendooven, J.; Devloo-Casier, K.; Levrau, E.; Van Hove, R.; Sree, S. P.; Baklanov, M. R.; Martens, J. A.; Detavernier, C. In Situ Monitoring of Atomic Layer Deposition in Nanoporous Thin Films Using Ellipsometric Porosimetry. *Langmuir* **2012**, *28* (8), 3852–3859.
- (23) Johnson, R. W.; Hultqvist, A.; Bent, S. F. A Brief Review of Atomic Layer Deposition: From Fundamentals to Applications. *Mater. Today* **2014**, *17* (5), 236–246.
- (24) Prasittichai, C.; Avila, J. R.; Farha, O. K.; Hupp, J. T. Systematic Modulation of Quantum (Electron) Tunneling Behavior by Atomic Layer Deposition on Nanoparticulate SnO<sub>2</sub> and TiO<sub>2</sub> Photoanodes. *J. Am. Chem. Soc.* **2013**, *135* (44), 16328–16331.
- (25) Sakai, N.; Ebina, Y.; Takada, K.; Sasaki, T. Electronic Band Structure of Titania Semiconductor Nanosheets Revealed by Electrochemical and Photoelectrochemical Studies. *J. Am. Chem. Soc.* **2004**, *126* (18), 5851–5858.
- (26) Ai, X.; Anderson, N. A.; Guo, J.; Lian, T. Electron Injection Dynamics of Ru Polypyridyl Complexes on SnO<sub>2</sub> Nanocrystalline Thin Films. *J. Phys. Chem. B* **2005**, *109* (15), 7088–7094.
- (27) Benkő, G.; Myllyperkio, P.; Pan, J.; Yartsev, A. P.; Sundstrom, V. Photoinduced Electron Injection from Ru(dcbpy)<sub>2</sub>(NCS)<sub>2</sub> to SnO<sub>2</sub> and TiO<sub>2</sub> Nanocrystalline Films. *J. Am. Chem. Soc.* **2003**, *125*, 1118–1119.
- (28) Anderson, N. A.; Ai, X.; Lian, T. Electron Injection Dynamics from Ru Polypyridyl Complexes to ZnO Nanocrystalline Thin Films. *J. Phys. Chem. B* **2003**, *107* (51), 14414–14421.
- (29) Sorantin, P.; Schwarz, K. Chemical Bonding in Rutile-Type Compounds. *Inorg. Chem.* **1992**, *31* (17), 567–576.
- (30) Beard, M. C.; Turner, G. M.; Schmittenmaer, C. A. Transient Photoconductivity in GaAs as Measured by Time-Resolved Terahertz Spectroscopy. *Phys. Rev. B: Condens. Matter Mater. Phys.* **2000**, *62* (23), 15764–15777.
- (31) Turner, G. M.; Beard, M. C.; Schmittenmaer, C. A. Carrier Localization and Cooling in Dye-Sensitized Nanocrystalline Titanium Dioxide. *J. Phys. Chem. B* **2002**, *106* (45), 11716–11719.
- (32) Baxter, J. B.; Schmittenmaer, C. A. Conductivity of ZnO Nanowires, Nanoparticles, and Thin Films Using Time-Resolved Terahertz Spectroscopy. *J. Phys. Chem. B* **2006**, *110* (50), 25229–25239.
- (33) Nemes, C. T.; Koenigsmann, C.; Schmittenmaer, C. A. Functioning Photoelectrochemical Devices Studied with Time-Resolved Terahertz Spectroscopy. *J. Phys. Chem. Lett.* **2015**, *6* (16), 3257–3262.
- (34) Furube, A.; Katoh, R.; Hara, K.; Murata, S.; Arakawa, H.; Tachiya, M. Ultrafast Stepwise Electron Injection from Photoexcited Ru-Complex into Nanocrystalline ZnO Film via Intermediates at the Surface. *J. Phys. Chem. B* **2003**, *107* (17), 4162–4166.
- (35) Furube, A.; Katoh, R.; Yoshihara, T.; Hara, K.; Murata, S.; Arakawa, H.; Tachiya, M. Ultrafast Direct and Indirect Electron-Injection Processes in a Photoexcited Dye-Sensitized Nanocrystalline Zinc Oxide Film: The Importance of Exciplex Intermediates at the Surface. *J. Phys. Chem. B* **2004**, *108* (33), 12583–12592.
- (36) McCool, N. S.; Swierk, J. R.; Nemes, C. T.; Saunders, T. P.; Schmittenmaer, C. A.; Mallouk, T. E. Proton-Induced Trap States, Injection and Recombination Dynamics in Water-Splitting Dye-Sensitized Photoelectrochemical Cells. *ACS Appl. Mater. Interfaces* **2016**, *8* (26), 16727–16735.
- (37) Parkinson, P.; Joyce, H. J.; Gao, Q.; Tan, H. H.; Zhang, X.; Zou, J.; Jagadish, C.; Herz, L. M.; Johnston, M. B. Carrier Lifetime and Mobility Enhancement in Nearly Defect-Free Core–Shell Nanowires Measured Using Time-Resolved Terahertz Spectroscopy. *Nano Lett.* **2009**, *9* (9), 3349–3353.
- (38) Boland, J. L.; Casadei, A.; Tütüncüoğlu, G.; Matteini, F.; Davies, C. L.; Jabeen, F.; Joyce, H. J.; Herz, L. M.; Fontcuberta i Morral, A.; Johnston, M. B. Increased Photoconductivity Lifetime in GaAs Nanowires by Controlled N-Type and P-Type Doping. *ACS Nano* **2016**, *10* (4), 4219–4227.